COMMUNICATION

Check for updates

A new halospinel superionic conductor for high-voltage all solid state lithium batteries†

Laidong Zhou, [iD] [a] Chun Yuen Kwok, [a] Abhinandan Shyamsunder, [a] Qiang Zhang, [iD] [b] Xiaohan Wu [c] and Linda F. Nazar [iD] *[a]

We report a new Li-superionic chloride, $Li_2Sc_{2/3}Cl_4$, that crystallizes in a disordered spinel structure, and exhibits an ionic conductivity of 1.5 mS cm^{-1} with a low activation energy barrier for Li$^+$ ion diffusion of 0.34 eV. This material is the first spinel-type superionic halide. Structural elucidation *via* powder neutron diffraction reveals a significantly disordered Li$^+$-ion distribution over available tetrahedral and octahedral sites within the lattice, forming an infinitely 3D connected Li$^+$ ion diffusion pathway comprised of face-sharing octahedra and tetrahedra. Due to the high oxidative stability of $Li_2Sc_{2/3}Cl_4$, all solid state lithium batteries employing $Li_2Sc_{2/3}Cl_4$ and high voltage cathodes ($LiCoO_2$, $LiNi_{0.6}Mn_{0.2}Co_{0.2}O_2$ or high-Ni $LiNi_{0.85}Mn_{0.1}Co_{0.05}O_2$) – without any coating – exhibit excellent electrochemical performance up to 4.6 V in terms of capacity retention and cycle life.

The evolution of lithium ion batteries (LIBs) from conventional LIBs (exploiting flammable liquid electrolytes and carbon anodes) to all solid state lithium batteries (ASSBs) using a solid electrolyte – and ideally a Li metal anode – could fundamentally eliminate safety concerns and provide higher energy density.[1–4] To realize the potential of ASSBs, a superionic conductive solid electrolyte (SE) (>1 mS cm^{-1}) with a wide electrochemical stability window is required.[5] Among a range of SE materials which have been studied,[6,7] sulfide materials generally exhibit high ionic conductivity approaching or even surpassing those of organic liquid electrolytes (>10 mS cm^{-1}), and a ductile nature. The latter makes it easier to minimize grain boundary resistance in the SE, and realize intimate contact between the solid electrolyte and active positive electrode (cathode) material. Thus sulfides have been a particular focus of research.[8–16] However, sulfides feature a low upper voltage stability window

Broader context

The evolution of lithium ion batteries – from conventional cell configurations that utilize flammable liquid electrolytes and low-density carbon anodes – to all solid state lithium batteries (ASSBs) employing a solid electrolyte, could fundamentally eliminate safety concerns and provide higher energy density due to better cell packing. To realize their potential, a ductile and superionic (>1 mS cm^{-1}) solid electrolyte (SE) with a wide electrochemical stability window is required. Importantly, SEs that exhibit good electrochemical and chemical stability with high-voltage lithium metal oxides obviate the need for protective coatings on the cathode. In this report, we describe a new halospinel ionic conductor, $Li_2Sc_{2/3}Cl_4$, which exhibits superionic conductivity of 1.5 mS cm^{-1}. Despite its name, scandium has an earth-abundance similar to lithium. This fast-ion conductive spinel halide, the first in its class, is prepared *via* a simple synthetic procedure and exhibits a mechanically soft nature. As proven by in-depth neutron diffraction studies, significant Li-site disorder in the lattice creates delocalized lithium-ion density and provides facile pathways for Li$^+$ diffusion. Most importantly, owing to its high oxidative stability, $Li_2Sc_{2/3}Cl_4$ exhibits excellent electrochemical performance in a potential window up to 4.6 V, combined with typical high voltage cathode materials ($LiCoO_2$, $LiNi_{0.6}Mn_{0.2}Co_{0.2}O_2$ and high-Ni $LiNi_{0.85}Mn_{0.1}Co_{0.05}O_2$), with no coatings.

(<2.5 V *vs.* Li/Li$^+$) which is not compatible with typical cathode materials ($LiCoO_2$, $LiNi_{1-x-y}Mn_xCo_yO_2$ (NMC)) in the absence of an insulating protective coating on the cathode particles.[17–20] Incorporation of sulfide SEs in ASSBs with bare $LiCoO_2$ or NMC leads to oxidation of the SE to form a passivating, blocking interphase.[21] The increase in internal resistance results in dramatic capacity fade.[22] Some oxide SEs such as garnets exhibit high ionic conductivity, good chemical stability with Li metal and a wide electrochemical stability window.[23,24] However, generally oxides are brittle, very difficult to process into SE/active material composites and can lead to high interfacial and grain boundary resistance. They also require high synthesis temperatures which are prohibitively costly, and are not amenable to cold (or elevated temperature) sintering. Thus it is still challenging to find SEs that can simultaneously meet all the requirements of superionic conductivity, a wide electrochemical window and good mechanical properties.

[a] *Department of Chemistry and the Waterloo Institute for Nanotechnology, University of Waterloo, 200 University Avenue West, Waterloo, Ontario N2L 3G1, Canada. E-mail: lfnazar@uwaterloo.ca*

[b] *Neutron Scattering Division, Oak Ridge National Laboratory, Oak Ridge, Tennessee 37830, USA*

[c] *BASF SE, Ludwigshafen 67056, Germany*

† Electronic supplementary information (ESI) available. See DOI: 10.1039/d0ee01017k

2056 | *Energy Environ. Sci.*, 2020, **13**, 2056–2063

This journal is © The Royal Society of Chemistry 2020

Recently, several lithium transition metal halides, including Li_3ErCl_6, Li_3YCl_6, Li_3InCl_6 and $Li_{3-x}M_{1-x}Zr_xCl_6$ (M = Er, Y) were reported with relatively high ionic conductivities of 0.31–1.49 mS cm^{-1} and a wide electrochemical window.[25–28] In poorly crystalline Li_3MCl_6 derived from mechanochemical milling, the increase in ionic conductivity (from $\sim 10^{-5}$ to 0.3 mS cm^{-1}) was ascribed to cation site disorder.[25] Substitution of Y (or Er) by Zr in crystalline Li_3MCl_6 induces a trigonal-to-orthorhombic phase transition and leads to much higher ionic conductivity (up to 1.4 mS cm^{-1}) than in the parent phases, accruing from distinctly different and more favourable Li-ion diffusion pathways.[28] The reason for the significantly increased ionic conductivity of Li_3InCl_6 compared to the value reported in 1992 (~ 0.01 mS cm^{-1}) is still unclear.[29] Although such materials are not stable with lithium because the transition metal cation in the halide can be easily reduced, Li_3YCl_6, Li_3InCl_6 and $Li_{3-x}M_{1-x}Zr_xCl_6$ (M = Er, Y) show very good compatibility with high voltage cathodes such as $LiCoO_2$.[26–28] In this regard, halides (specifically chlorides, which possesses higher anodic stability than bromides and iodides) are attractive for applications in high voltage ASSBs. Until now, very limited materials have been reported with ionic conductivity >1 mS cm^{-1}. Thus it is essential to search for other halides that could exhibit such promising properties. Materials with a spinel structure, including Li_2MgCl_4 and Li_2ZnCl_4, were studied in the 1970–1980s.[30–33] However, these spinel chlorides exhibit extremely low ionic conductivity ($<10^{-3}$ mS cm^{-1} at room temperature), and thus cannot be used as SEs in ASSBs.

Herein, we report on a new disordered-spinel chloride superionic conductor, $Li_2Sc_{2/3}Cl_4$, which exhibits a superionic conductivity of 1.5 mS cm^{-1} and is based on the relatively more abundant element scandium (despite its name) compared to indium or erbium. The spinel is prepared *via* a simple synthetic procedure, unlike Li_3YCl_6 and Li_3ErCl_6 which require long duration high energy ball-milling to reach a conductivity of

0.3 mS cm^{-1}. $Li_2Sc_{2/3}Cl_4$ represents the first spinel-type superionic conductor, due to significant Li-site disorder in the lattice as determined by neutron diffraction studies that fully refine the structure. Delocalized lithium-ion density serves as interstitial sites that provide critical Li^+ ion diffusion pathways, similar to other superionic conductors.[8,23,34] Importantly, $Li_2Sc_{2/3}Cl_4$ exhibits excellent electrochemical performance combined with typical high voltage cathode materials with a bare surface ($LiCoO_2$, $LiNi_{0.6}Mn_{0.2}Co_{0.2}O_2$ and high-Ni $LiNi_{0.85}Mn_{0.1}Co_{0.05}O_2$; no coatings applied) due to their stable interface formed with this halide SE and its mechanically pliable and high oxidative stable nature. Cells cycled at room temperature with a high upper cutoff voltage between 4.3 and 4.6 V exhibit stable behaviour for over 70–110 cycles and capacity up to 215 mA h g^{-1} at a C/5 rate.

Structural evolution of disordered spinel $Li_2Sc_{2/3}Cl_4$

X-ray diffraction (Fig. 1a, red pattern) shows that the targeted synthesis of spinel $Li_2Sc_{2/3}Cl_4$ provides almost phase-pure polycrystalline powder with only a trace amount of unknown impurities. Preparing the material for XRD analysis revealed its soft and ductile nature. The pattern was indexed in the same cubic space group, $Fd\bar{3}m$ which is adopted by other spinel materials. A lower Sc^{3+} content leads to increasing amounts of LiCl impurity, as shown in Fig. 1a, black pattern. A slightly higher Sc^{3+} content leads to lower ionic conductivity (see below) and even higher Sc^{3+} content leads to a $ScCl_3$ impurity (Fig. S1, ESI†). The title composition is therefore optimal. The structure of spinel $Li_2Sc_{2/3}Cl_4$ was determined from Rietveld refinement of the time of flight powder neutron diffraction pattern, as shown in Fig. 1b and the crystallographic details are summarized in Table 1. The framework is somewhat similar to the previously reported spinel Li_2MgCl_4.[30] The important difference is that the
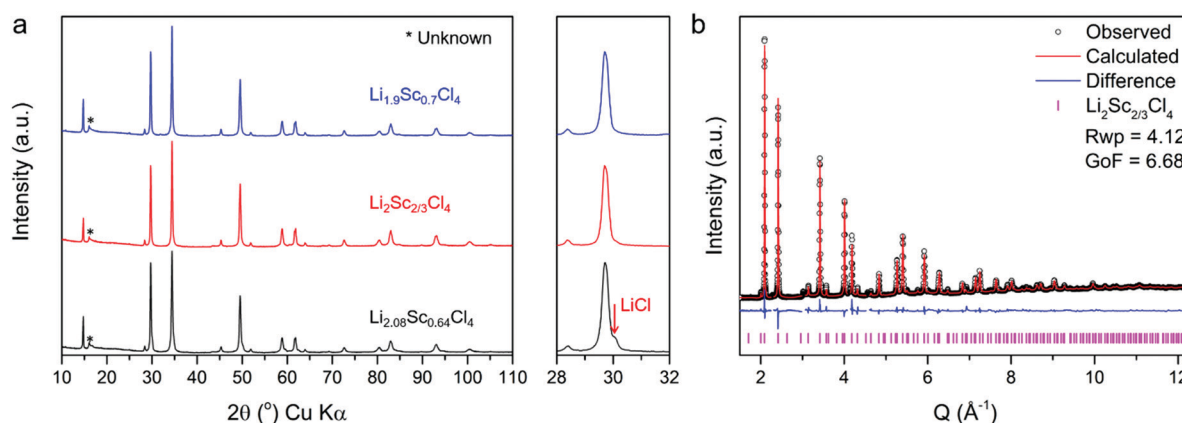

Fig. 1 (a) Powder X-ray diffraction patterns of $Li_{2.08}Sc_{0.64}Cl_4$ (black), $Li_2Sc_{2/3}Cl_4$ (red) and $Li_{1.9}Sc_{0.7}Cl_4$ (blue). All reflections correspond to the respective spinel phase except for the unknown impurity as marked; red arrows indicate LiCl impurity. (b) Time-of-flight neutron diffraction and the corresponding Rietveld refinement fit of $Li_2Sc_{2/3}Cl_4$, excluded regions (Q = 2.28, 3.01, 4.11 and 4.56 Å^{-1}) correspond to trace unknown impurity phase. Experimental data are shown in black circles; the red line denotes the calculated pattern; the difference profile is shown in blue and calculated positions of the Bragg reflections are shown as vertical ticks. R_{wp} and GoF are the weighted profile R-factor and goodness of fit respectively.

Table 1 Atomic coordinates, occupation factor, and isotropic displacement parameter of $Li_2Sc_{2/3}Cl_4$ obtained from time-of-flight powder neutron diffraction at 300 K

$a = 10.4037(5)$ Å, space group: $Fd\bar{3}m$						
Atom	Wyckoff site	x	y	z	Occupancy	U_{iso} (Å²)
Li1 tet	8a	0.125	0.125	0.125	0.141(27)	0.025(20)
Li2 oct	16c	0	0	0	0.218(13)	0.038(5)
Li3 tet	48f	0.125	0.125	0.886(16)	0.0282(63)	0.025
Li4 oct	16d	0.5	0.5	0.5	0.689(2)	0.0029(6)
Sc1	16d	0.5	0.5	0.5	0.311(2)	0.0029(6)
Cl1	32e	0.25435(6)	0.25435(6)	0.25435(6)	1	0.0208(2)
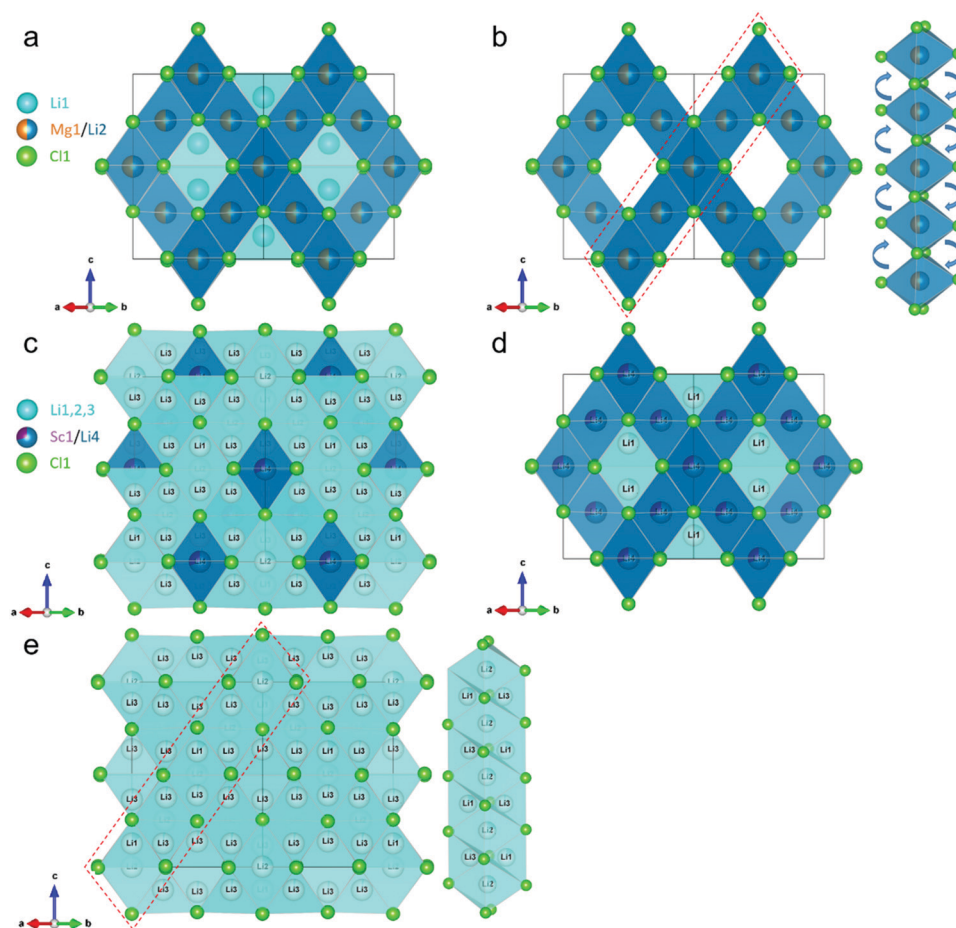
Fig. 2 (a) Structure of spinel Li_2MgCl_4 from single crystal X-ray diffraction reported in ref. 33 and (b) structure of spinel Li_2MgCl_4 (corner-sharing $Li(1)Cl_4$ tetrahedra are not shown) depicting a possible Li^+ ion diffusion pathway formed by edge-shared $(Mg1/Li2)Cl_6$ octahedra whose faces border empty tetrahedral sites (enlarged); $Li(1)Cl_4$ – (light blue) tetrahedra and $(Mg1/Li2)Cl_6$ – (dark blue) octahedra. (c) structure of disordered spinel $Li_2Sc_{2/3}Cl_4$ from TOF powder neutron diffraction and (d) structure without illustrating $Li(2)Cl_6$ octahedra and $Li(3)Cl_4$ tetrahedra, demonstrating that it is related to spinel Li_2MgCl_4 but with different site occupancies. $(Sc1/Li_4)Cl_6$ octahedra are in dark blue and $Li(1)Cl_4$ tetrahedra in light blue; (e) structure of disordered spinel $Li_2Sc_{2/3}Cl_4$ only showing face-sharing $Li(1,3)Cl_4$ tetrahedra and $Li(2)Cl_6$ octahedra that represent a 3D Li^+ ion diffusion pathway; expansion shows potential ion diffusion through $Li(2)Cl_6$ octahedra passing by $Li(1,3)Cl_4$ tetrahedra.

disordered spinel $Li_2Sc_{2/3}Cl_4$ exhibits four Li sites: Li2 and Li3 are new while Li1 and Li4 are also present in Li_2MgCl_4, as shown in Fig. 2a, c and d. Li_2MgCl_4 is constructed from edge-sharing $(Mg1/Li2)Cl_6$ octahedra (Fig. 2b) and Li1 fills the corner-sharing tetrahedral site (Fig. 2a). In contrast, while $Li_2Sc_{2/3}Cl_4$ also contains edge-sharing $(Sc1/Li4)Cl_6$ octahedra, Li1,2,3 occupy the face-sharing octahedral and tetrahedral sites (Fig. 2c–e).

Ionic conductivity and Li^+ ion diffusion pathways

Temperature-dependent impedance spectroscopy measurements were performed to determine the ionic conductivity of cold-pressed $Li_2Sc_{2/3}Cl_4$ and the activation energy for Li^+ ion transport (Fig. 3). The corresponding impedance responses (illustrated as Nyquist plots) are shown in Fig. 3a and b. $Li_2Sc_{2/3}Cl_4$ exhibits

2058 | *Energy Environ. Sci.*, 2020, **13**, 2056–2063

This journal is © The Royal Society of Chemistry 2020

superionic conductivity of 1.5 mS cm^{-1} at room temperature. The Nyquist plots at different temperatures were fit to derive ionic conductivity values that were used for the corresponding Arrhenius plot, yielding a low activation energy, E_a = 0.336 eV (Fig. 3c). Li$_{2.08}$Sc$_{0.64}$Cl$_4$ exhibits a slightly lower ionic conductivity of 1.22 mS cm^{-1} due to minor LiCl impurities and Li$_{1.9}$Sc$_{0.7}$Cl$_4$ also exhibits a lower ionic conductivity of 1.09 mS cm^{-1} due to a lower carrier concentration (Fig. S2, ESI†).

The ionic conductivity of the new disordered spinel, Li$_2$Sc$_{2/3}$Cl$_4$, is more than three orders of magnitude higher than previously reported chlorospinels including Li$_2$MCl$_4$ (M = Mg, V, Cr, Mn, Fe, Co, Zn, Cd) which exhibit very low ionic transport, σ_i < 10^{-3} mS cm^{-1}.[30–33,35] As described above, the difference is that Li$_2$Sc$_{2/3}$Cl$_4$ exhibits multiple Li sites in the spinel lattice (and two new Li sites) compared to the other materials. Taking Li$_2$MgCl$_4$ as an example, Li$^+$ ions would likely diffuse through the faces of edge-shared Li(2)Cl$_6$ octahedra that border an empty tetrahedral site (Fig. 2b). While the Li2 site is also a shared site with Mg^{2+} (half occupied by both Mg^{2+} and Li$^+$), both Li1 and Li2 sites are fully occupied. Hence a defect formation step is necessary to sustain macroscopic Li$^+$ ion diffusion. Furthermore, divalent Mg^{2+} is present within the main diffusion pathway, which will hinder Li$^+$ ion diffusion due to its presumed low mobility.[36] The sum of these factors result in the high activation energy and low ionic conductivity previously reported.[32] For the disordered spinel Li$_2$Sc$_{2/3}$Cl$_4$, the same possible (Sc/Li4)Cl$_6$ octahedral pathway (via empty face-shared sites described in Fig. 2b for Li$_2$MgCl$_4$) also exists, illustrated in Fig. 2d. However, trivalent Sc^{3+} ions also sit within the pathway and are anticipated to block Li$^+$ ion diffusion; thus Li$^+$ ions in this site will have very low mobility, as supported by their very low atomic displacement parameter (Table 1). This Li/Sc shared site forms a rigid framework that allows the diffusion of Li$^+$ ions resident on the other sites. The additional Li$^+$ ions are spread over the other face-sharing octahedral and tetrahedral Li1,2,3 sites, which form a proposed, infinite 3D Li$^+$ ion diffusion pathway displayed in Fig. 2e. The relatively low occupancy of the Li1,2,3 sites result in vacancies which help eliminate the defect formation step for Li$^+$ ion diffusion. The re-distribution of Li$^+$-ion density over available tetrahedral and octahedral sites within the lattice suggests the Li site energies are relatively similar which would lead to a relatively flat energy landscape for Li$^+$ ion diffusion.[8,23,34] Overall, the relatively low activation energy is supported by the new probable diffusion pathway and considerable vacancies that promote Li$^+$ ion mobility.

Electrochemical performance

Bulk-type ASSBs with Li$_2$Sc$_{2/3}$Cl$_4$ as a solid electrolyte, using uncoated high voltage cathode materials (bare-LiCoO$_2$ and bare-NMC622 or NMC85) and Li–In alloy as the negative electrode, were constructed to demonstrate the electrochemical performance of this new chlorospinel solid electrolyte. Li–In alloy was chosen as the negative electrode because Sc^{3+} can be reduced by Li (in Fig. S3, ESI†). A highly-superionic conductive sulfide solid electrolyte layer (Li$_{6.7}$Si$_{0.7}$Sb$_{0.3}$S$_5$I, 12.6 mS cm^{-1})[8] was added between the Li–In alloy and Li$_2$Sc$_{2/3}$Cl$_4$ layer to further prevent the reduction of Li$_2$Sc$_{2/3}$Cl$_4$ and decrease the total cell resistance. Bulk-type ASSBs show very good performance in terms of coulombic efficiency and cycling performance (Fig. 4 and 5). In large part, this owes to the high oxidative stability of Li$_2$Sc$_{2/3}$Cl$_4$ as indicated by linear sweep voltammetry (LSV) performed on chlorospinel electrodes mixed with 30 wt% Super P carbon (Fig. S4a, ESI†). The ultra-slow sweep (0.01 mV s^{-1}), which effectively probes the equilibrium potential limit, suggests that Li$_2$Sc$_{2/3}$Cl$_4$ is thermodynamically stable up to ∼4.3 V vs. Li$^+$/Li (and kinetically beyond, see below), i.e., very much higher than sulfide materials (2.5 V).[17] The initial charge/discharge curves of LCO and NMC622 cells cycled in different voltage ranges, up to 4.5 V vs. Li$^+$/Li are shown in Fig. S4b and c (ESI†). All cells exhibit high initial coulombic efficiency >93.7%, which indicates the Li$_2$Sc$_{2/3}$Cl$_4$ chlorospinel is stable with these high voltage cathode materials. Fig. S5 (ESI†) shows the cross-section of ASSBs after cycling (fully discharged state) which reveals that the NMC622 and LiCoO$_2$ particles are well embedded in the Li$_2$Sc$_{2/3}$Cl$_4$ matrix and achieve excellent contact. The LCO cell exhibits excellent rate capacity (Fig. 4a and b). With an upper cutoff voltage of 4.3 V vs. Li$^+$/Li, the cell exhibits a high initial discharge capacity of
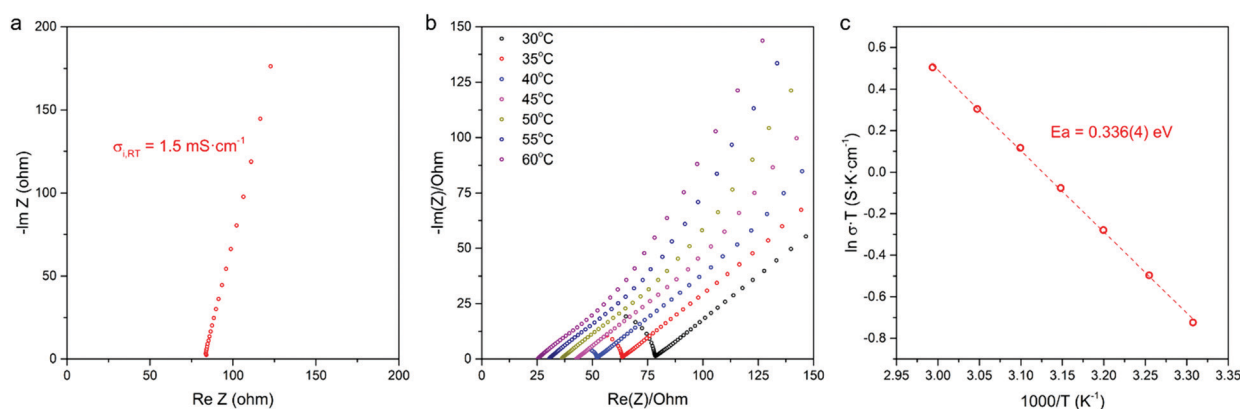

Fig. 3 Nyquist plots of Li$_2$Sc$_{2/3}$Cl$_4$ (a) at room temperature and (b) at each temperature used to determine activation energy; (c) Arrhenius plots of the conductivity values for Li$_2$Sc$_{2/3}$Cl$_4$ in the temperature range from 30 to 60 °C.
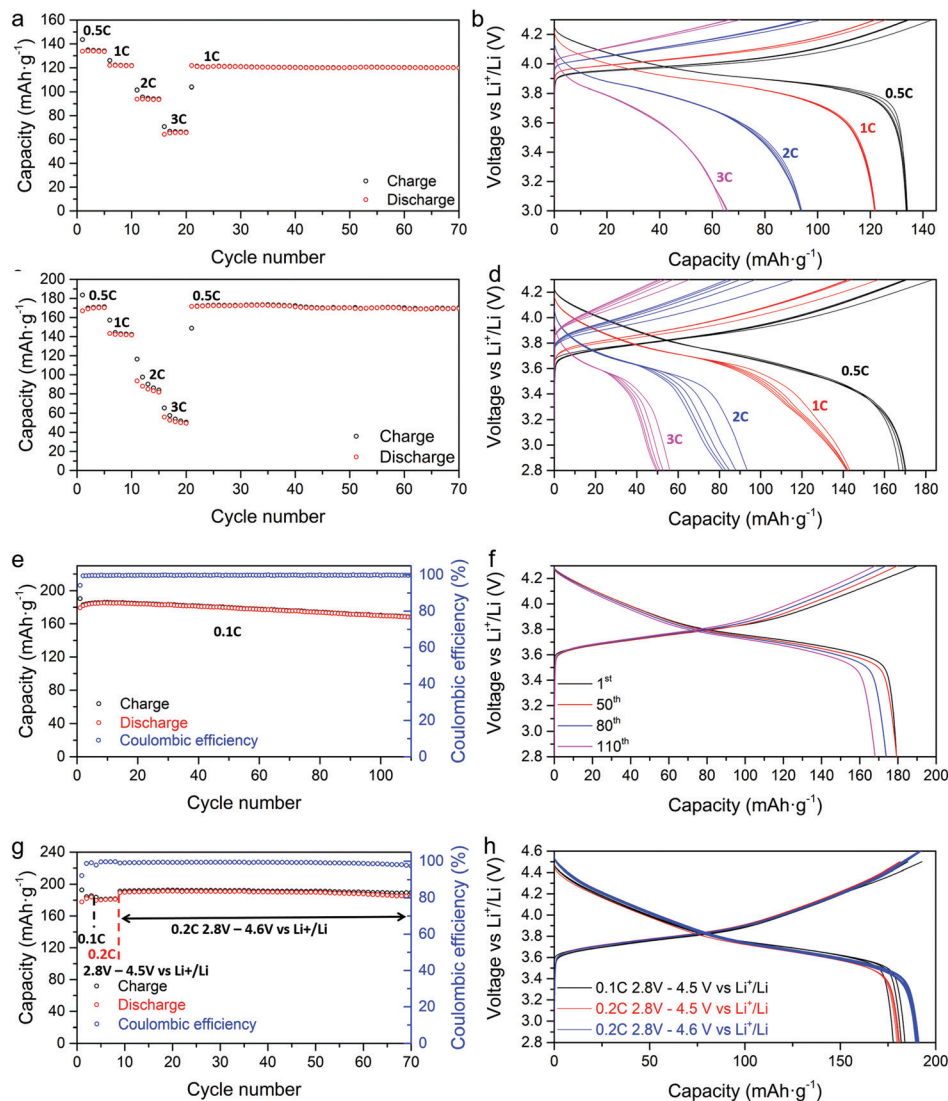
Fig. 4 Electrochemical performance of $LiCoO_2$ and NMC622 ASSBs using $Li_2Sc_{2/3}Cl_4$ as the solid electrolyte at room temperature. Charge−discharge capacity as a function of cycle number at different C-rates for (a) $LCoO_2$ ASSB and (c) NMC622 ASSB and corresponding charge−discharge curves at different C-rates for (b) $LiCoO_2$ ASSB and (d) NMC622 ASSB. (e) Charge−discharge capacity and the coulombic efficiency (CE) as a function of cycle number for NMC 622 ASSB cycled at 0.1C between 2.8 V and 4.3 V vs. Li^+/Li and (f) corresponding charge−discharge curves. (g) Charge−discharge capacity and the coulombic efficiency (CE) as a function of cycle number for NMC622 ASSB cycled at 0.1C, 0.2C between 2.8 V, 4.5 V and 4.6 V vs. Li^+/Li and (h) corresponding charge−discharge curves.

135 mA h g^{-1} at a 0.5C rate (Fig. 4b) and good capacity retention. Even at 1C, the cell still retains a reversible capacity over 120 mA h g^{-1} (Fig. 4a and Fig. S6a, ESI†), which is significantly better than those of state-of-art $LiCoO_2$ ASSBs.[37–39] Fig. S7 (ESI†) shows the initial and final EIS data of the corresponding LCO cells in Fig. 4a. The total impedance of cells cycled at fast rates are almost same as the initial state, which further demonstrates the excellent high voltage stability of $Li_2Sc_{2/3}Cl_4$.

The NMC622 cell also exhibits good rate capability (Fig. 4c, d and Fig. S6b, ESI†), although slightly inferior to the LCO cell described above, possibly due to the microstructure of NMC622 particles that contains randomly oriented grains (i.e., small primary particles aggregated into large secondary particles).[40] In comparison, LCO is comprised of large single $LiCoO_2$

crystallites (Fig. S8, ESI†). Tuning cathode particle size and microstructure will potentially further improve the electrochemical performance of NMC-type ASSBs.[40–43] Fig. 4e and f show the long-term cycling of the NMC622 cell at 0.1C between 2.8 V and 4.3 V vs. Li^+/Li. It exhibits very stable capacity retention with very little capacity fade, maintaining a capacity of ∼170 mA h g^{-1} after 110 cycles with high coulombic efficiency; ∼99.8% on average. The NMC622 cell also exhibits excellent cycling performance with a cutoff voltage of 4.6 V (vs. Li^+/Li) with very low capacity fade. It maintains a capacity of ∼190 mA h g^{-1} with high coulombic efficiency of ∼99.6% on average at 0.2C over 70 cycles (Fig. 4g); typical voltage profiles are shown in Fig. 4h. This performance is significantly better than previously reported ASSBs with typical coated NMC cathodes
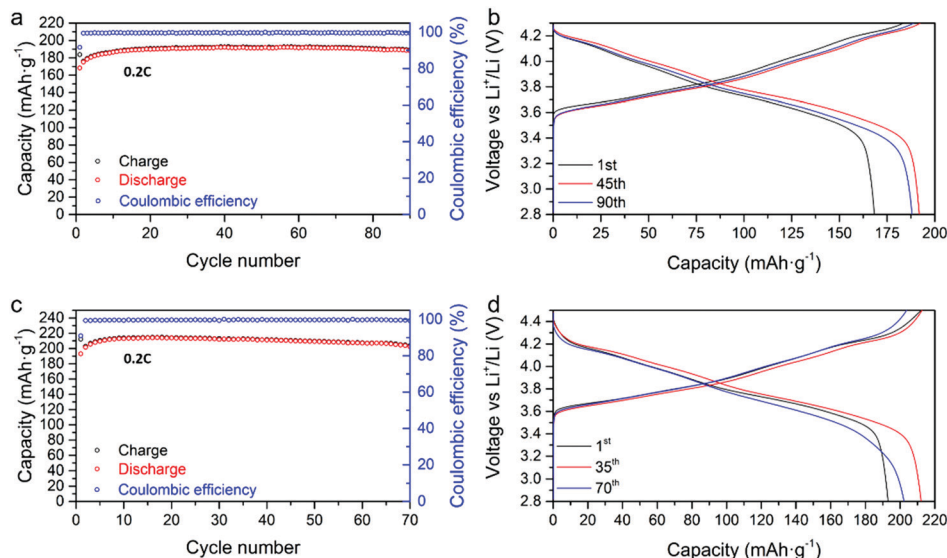
2060 | Energy Environ. Sci., 2020, **13**, 2056–2063

This journal is © The Royal Society of Chemistry 2020

Fig. 5 Electrochemical performance of NMC85 ASSBs using $Li_2Sc_{2/3}Cl_4$ as the solid electrolyte at room temperature. Charge–discharge capacity and the coulombic efficiency (CE) as a function of cycle number for NMC85 ASSBs cycled at 0.2C (a) between 2.8 V and 4.3 V and (c) between 2.8 V and 4.5 V vs. Li^+/Li and (b) and (d) corresponding charge–discharge curves.

married with a sulfide SE.[44] This data suggests that while the thermodynamic stability of $Li_2Sc_{2/3}Cl_4$ is ~4.3 V vs. Li^+/Li, in fact, a kinetically quasi-stable interface forms between NMC622 and $Li_2Sc_{2/3}Cl_4$ up to 4.6 V. The exact nature of this interface will be explored in future studies.

High-Ni NMC ($LiNi_{0.85}Mn_{0.1}Co_{0.05}O_2$) cathode materials provide even higher capacity, which can further improve the energy density of ASSBs. With an upper cutoff voltage of 4.3 V vs. Li^+/Li, cells exhibit a stable discharge capacity > 190 mA h g^{-1} at a rate of 0.2C and good capacity retention for 90 cycles (Fig. 5a and b). NMC85 cells cycled with a high upper cutoff voltage of 4.5 V also exhibit stable cycling with high discharge capacity up to 214 mA h g^{-1} at 0.2C and good capacity retention for 70 cycles (Fig. 5c and d). These findings represent the first 4.5 V NMC85 ASSBs with stable performance. Typically, NMC85 cells with liquid electrolytes show capacity fade when charged to high potential.[45–47] This is due to the surface of NMC85 particles being converted to spinel and rock-salt types phases, and formation of a cathode-electrolyte interface (owing to the oxidation of liquid electrolyte by the strongly oxidizing $Ni^{3+/4+}$ sites) which impedes Li ion diffusion.[48–50] The excellent cycling of NMC85 ASSBs is likely due to the good oxidative stability of $Li_2Sc_{2/3}Cl_4$, as no Li ion blocking interface is built up between the contact of the NMC and $Li_2Sc_{2/3}Cl_4$. Nonetheless, the intrinsic nature of high-Ni NMC materials and their aggregate microstructure (Fig. S9, ESI†) undoubtedly leads to the very slow capacity fading in NMC ASSBs, exhibited in Fig. 5. This may be due to Ni migration/phase transformation at high potential, and micro-cracks formed in cycled NMC particles due to the volume change during cycling that can create loss of contact within the electrode.

In addition to being employed as a solid electrolyte in ASSBs, $Li_2Sc_{2/3}Cl_4$ can be also utilized as a high voltage cathode coating

material, where the coated cathode materials can be used with lower-cost sulfide solid electrolytes. Overall, the excellent electrochemical performance of ASSBs employing this novel $Li_2Sc_{2/3}Cl_4$ solid electrolyte and a >4 V voltage uncoated NMC or LCO cathode highlights its high room temperature Li^+ ion conductivity and oxidative stability window, which bodes well for practical applications of ASSBs.

Conclusions

In summary, we have synthesized a new superionic chloride, $Li_2Sc_{2/3}Cl_4$, with a disordered spinel structure and high Li^+ ion conductivity of 1.5 mS cm^{-1}, representing the first spinel structure superionic conductor. Excellent electrochemical performance is observed for bulk-type ASSBs with bare $LiCoO_2$ or NMC cathode materials (no external coating) at potentials up to 4.6 V, which augers well for the future development of advanced high energy density and stable cycling life ASSBs. Most importantly, while we report the first spinel superionic conductors, multiple elemental doping can be conducted to further increase the ionic conductivity. The same concept can be applied to other Li-spinel structured ion conductors including sulfides and oxides, which introduces a new avenue in developing new solid electrolytes for all solid state batteries.

Conflicts of interest

The authors declare no competing interests.

Acknowledgements

Energy & Environmental Science

Communication

References

1 J. Janek and W. G. Zeier, *Nat. Energy*, 2016, **1**, 16141.

2 S. Randau, D. A. Weber, O. Kotz, R. Koerver, P. Braun, A. Weber, E. I. Tiffee, T. Adermann, J. Kulish, W. G. Zeier, F. H. Richter and J. Janek, *Nat. Energy*, 2020, **5**, 259–270.

3 R. Chen, Q. Li, X. Yu, L. Chen and H. Li, *Chem. Rev.*, 2019, DOI: 10.1021/acs.chemrev.9b00268.

4 D. H. S. Tan, A. Banerjee, Z. Chen and Y. S. Meng, *Nat. Nanotechnol.*, 2020, **15**, 170–180.

5 A. Manthiram, X. Yu and S. Wang, *Nat. Rev. Mater.*, 2017, **2**, 16103–16118.

6 J. C. Bachman, S. Muy, A. Grimaud, H. H. Chang, N. Pour, S. F. Lux, O. Paschos, F. Maglia, S. Lupart, P. Lamp, L. Giordano and S. H. Yang, *Chem. Rev.*, 2016, **116**, 140–162.

7 Z. Zhang, Y. Shao, B. Lotsch, Y. S. Hu, H. Li, J. Janek, L. F. Nazar, C. W. Nan, J. Maier, M. Armand and L. Chen, *Energy Environ. Sci.*, 2018, **11**, 1945–1976.

8 L. Zhou, A. Assoud, Q. Zhang, X. Wu and L. F. Nazar, *J. Am. Chem. Soc.*, 2019, **141**, 19002–19013.

9 N. Kamaya, K. Homma, Y. Yamakawa, M. Hirayama, R. Kanno, M. Yonemura, T. Kamiyama, Y. Kato, S. Hama, K. Kawamoto and A. Mitsui, *Nat. Mater.*, 2011, **10**, 682–686.

10 Y. Kato, S. Hori, T. Saito, K. Suzuki, M. Hirayama, A. Mitsui, M. Yonemura, H. Iba and R. Kanno, *Nat. Energy*, 2016, **1**, 16030.

11 M. A. Kraft, S. Ohno, T. Zinkevich, R. Koerver, S. P. Culver, T. Fuchs, A. Senyshyn, S. Indris, B. J. Morgan and W. G. Zeier, *J. Am. Chem. Soc.*, 2018, **140**, 16330–16339.

12 L. Zhou, K. H. Park, X. Sun, F. Lalere, T. Adermann, P. Hartmann and L. F. Nazar, *ACS Energy Lett.*, 2019, **4**, 265–270.

13 I. H. Chu, H. Nguyen, S. Hy, Y. C. Lin, Z. Wang, Z. Xu, Z. Deng, Y. S. Meng and S. P. Ong, *ACS Appl. Mater. Interfaces*, 2016, **8**, 7843–7853.

14 J. M. Doux, Y. Yang, D. H. S. Tan, H. Nguyen, E. A. Wu, X. Wang, A. Banerjee and Y. S. Meng, *J. Mater. Chem. A*, 2020, **8**, 5049–5055.

15 M. Sokseiha, V. Johannes, S. Roman, K. Raimund, S. J. Stefan, M. Filippo, L. Peter, W. G. Zeier and S. H. Yang, *iScience*, 2019, **16**, 270–282.

16 M. Sokseiha, J. C. Bachman, L. Giordano, H. H. Chang, D. L. Abernathu, D. Bansal, O. Delaire, S. Hori, R. Kanno, F. Maglia, S. Lupart, P. Lamp and S. H. Yang, *Energy Environ. Sci.*, 2018, **11**, 850–859.

17 W. D. Richards, L. J. Miara, Y. Wang, J. C. Kim and G. Ceder, *Chem. Mater.*, 2015, **28**, 266–273.

18 Y. Xiao, Y. Wang, S. H. Bo, J. C. Kim, L. J. Miara and G. Ceder, *Nat. Rev. Mater.*, 2020, **5**, 105–126.

19 D. H. S. Tan, E. A. Wu, H. Nguyen, Z. Chen, M. A. T. Marple, J. M. Doux, X. Wang, H. Yang, A. Banerjee and Y. S. Meng, *ACS Energy Lett.*, 2019, **4**, 2418–2427.

20 J. M. Doux, H. Nguyen, D. H. S. Tan, A. Banerjee, X. Wang, E. A. Wu, C. Jo, H. Yang and Y. S. Meng, *Adv. Energy Mater.*, 2020, **10**, 1903253.

21 A. Banerjee, H. Tang, X. Wang, J. H. Cheng, H. Nguyen, M. Zhang, D. H. S. Tan, T. A. Wynn, E. A. Wu, J. M. Doux, T. Wu, L. Ma, G. E. Sterbinsky, M. S. Dsouza, S. P. Ong and Y. S. Meng, *ACS Appl. Mater. Interfaces*, 2019, **11**, 43138–43145.

22 W. Zhang, F. H. Richter, S. P. Culver, T. Leichtweiss, J. G. Lozano, C. Dietrich, P. G. Bruce, W. G. Zeier and J. Janek, *ACS Appl. Mater. Interfaces*, 2018, **10**, 22226–22236.

23 A. J. Samson, K. Hofstetter, S. Bag and V. Thangadurai, *Energy Environ. Sci.*, 2019, **12**, 2957–2975.

24 H. Buschmann, J. Dolle, S. Berendts, A. Kuhn, P. Bottke, M. Wilkening, P. Heitjans, A. Senyshyn, H. Ehrenberg, A. Lotnyk, V. Duppel, L. Kienle and J. Janek, *Phys. Chem. Chem. Phys.*, 2011, **13**, 19378–19392.

25 R. Schlem, S. Muy, N. Prinz, A. Banik, S. H. Yang, M. Zobel and W. G. Zeier, *Adv. Energy Mater.*, 2020, **10**, 1903719.

26 T. Asano, A. Sakai, S. Ouchi, M. Sakaida, A. Miyazaki and A. Hasegawa, *Adv. Mater.*, 2018, **30**, 1803075.

27 X. Li, J. Liang, J. Luo, M. N. Banis, C. Wang, W. Li, S. Deng, C. Yu, F. Zhao, Y. Hu, T. K. Sham, L. Zhang, S. Zhao, S. Lu, H. Huang, R. Li, K. R. Adair and X. Sun, *Energy Environ. Sci.*, 2019, **12**, 2665.

28 K. H. Park, K. Kaup, A. Assoud, Q. Zhang, X. Wu and L. F. Nazar, *ACS Energy Lett.*, 2020, **5**, 533–539.

29 H. J. Steiner and H. Lutz, *Z. Anorg. Allg. Chem.*, 1992, **613**, 26–30.

30 C. J. J. Van Loon and J. deLong, *Acta Crystallogr.*, 1975, **B31**, 2549.

31 H. D. Lutz, W. Schmidt and H. Haeuseler, *J. Phys. Chem. Solids*, 1981, **42**, 287–289.

32 R. Kanno, Y. Takeda and O. Yamamoto, *Solid State Ionics*, 1986, **28–30**, 1276–1281.

33 M. Partik, M. Schneider and H. D. Lutz, *Z. Anorg. Allg. Chem.*, 1994, **620**, 791–795.

34 L. Zhou, A. Assoud, A. Shyamsunder, A. Huq, Q. Zhang, P. Hartmann, J. Kulisch and L. F. Nazar, *Chem. Mater.*, 2019, **31**, 7801–7811.

35 C. Cros, L. Hanebali, L. Latie, G. Villeneuve and W. Gang, *Solid State Ionics*, 1983, **9–10**, 139–147.

36 P. Canepa, S. H. Bo, G. S. Gautam, B. Key, W. D. Richards, T. Shi, Y. Tian, Y. Wang, J. Li and G. Ceder, *Nat. Commun.*, 2017, **8**, 1759.

37 K. H. Park, D. Y. Oh, Y. E. Choi, Y. J. Nam, L. Han, J. Kim, H. Xin, F. Lin, S. M. Oh and Y. S. Jung, *Adv. Mater.*, 2015, **28**, 1874–1883.

38 W. Zhang, D. A. Weber, H. Weigand, T. Arlt, I. Manke, D. Schroder, R. Koerver, T. Leichtweiss, P. Hartmann, W. G. Zeier and J. Janek, *ACS Appl. Mater. Interfaces*, 2017, **9**, 17835–17845.

39 S. H. Jung, K. Oh, Y. J. Nam, D. Y. Oh, P. Bruner, K. Kang and Y. S. Jung, *Chem. Mater.*, 2018, **30**, 8190–8200.

40 S. H. Jung, U. H. Kim, J. H. Kim, S. Jun, C. S. Yoon, Y. S. Jung and Y. K. Sun, *Adv. Energy Mater.*, 2019, 1903360.

41 T. Shi, Q. Tu, Y. Tian, Y. Tian, L. J. Miara, O. Kononova and G. Ceder, *Adv. Energy Mater.*, 2020, **10**, 1902881.

42 F. Strauss, T. Bartsch, L. de Biasi, A. Y. Kim, J. Janek, P. Hartmann and T. Brezesinski, *ACS Energy Lett.*, 2018, **3**, 992–996.

2062 | *Energy Environ. Sci.*, 2020, **13**, 2056–2063

This journal is © The Royal Society of Chemistry 2020

43 A. Bielefeld, D. A. Weber and J. Janek, *J. Phys. Chem. C*, 2019, **123**, 1626–1634.

44 A. Y. Kim, F. Strauss, T. Bartsch, J. H. Teo, T. Hatsukade, A. Mazikin, J. Janek, P. Hartmann and T. Brezesinsk, *Chem. Mater.*, 2019, **31**, 9664–9672.

45 F. A. Susai, H. Sclar, S. Maiti, L. Burstein, O. Perkal, J. Grinblat, M. Talianker, S. Ruthstein, C. Erk, P. Hartmann, B. Markovsky and D. Aurbach, *ACS Appl. Energy Mater.*, 2020, **3**, 3609–3618.

46 S. Schweidler, L. de Biasi, G. Garcia, A. Mazilkin, P. Hartmann, T. Brezesinski and J. Janek, *ACS Appl. Mater. Interfaces*, 2019, **2**, 7375–7384.

47 S. Schweidler, L. de Biasi, P. Hartmann, T. Brezesinski and J. Janek, *ACS Appl. Mater. Interfaces*, 2020, **3**, 2821–2827.

48 H. H. Sun, H. Ryu, U. Kim, J. A. Weeks, A. Heller, Y. K. Sun and C. B. Mullins, *ACS Energy Lett.*, 2020, **5**, 1136–1146.

49 R. Tatara, Y. Yu, P. Karayaylali, A. K. Chan, Y. Zhang, R. Jung, F. Maglia, L. Giordano and S. H. Yang, *ACS Appl. Mater. Interfaces*, 2019, **11**, 34973–34988.

50 L. Yin, Z. Li, G. S. Mattei, J. Zheng, W. Zhao, F. Omenya, C. Fang, W. Li, J. Li, Q. Xie, E. M. Erickson, J. G. Zhang, M. S. Whittingham, Y. S. Meng, A. Manthiram and P. G. Khalifah, *Chem. Mater.*, 2020, **32**, 1002–1010.

This journal is © The Royal Society of Chemistry 2020

Energy Environ. Sci., 2020, **13**, 2056–2063 | **2063**